2013

Novel Nanostructured Rare-Earth-Free Magnetic Materials with High Energy Products

Balamurugan Balasubramanian
University of Nebraska–Lincoln, balamurugan@unl.edu

Bhaskar Das
University of Nebraska–Lincoln, bhaskar.das@huskers.unl.edu

Ralph Skomski
University of Nebraska-Lincoln, rskomski2@unl.edu

Wenyong Zhang
University of Nebraska–Lincoln, wenyong.zhang@unl.edu

David J. Sellmyer
University of Nebraska-Lincoln, dsellmyer@unl.edu

Published in *Advanced Materials* 25 (2013), pp. 6090–6093; doi: 10.1002/adma.201302704

Submitted June 13, 2013; published online August 19, 2013.

Supporting information for this article is available following the references.

Novel Nanostructured Rare-Earth-Free Magnetic Materials with High Energy Products

Balamurugan Balasubramanian, Bhaskar Das, Ralph Skomski,

Wenyong Y. Zhang, and David J. Sellmyer

Nebraska Center for Materials and Nanoscience and the Department of Physics and Astronomy, University of Nebraska–Lincoln, Lincoln, NE 68588, USA

Dr. B. Balasubramanian and Bhaskar Das contributed equally to this work.

Corresponding authors – Balamurugan Balasubramanian, USA email bbalasubramanian2@unl.edu and David J. Sellmyer, email dsellmyer@unl.edu

The development of new iron- or cobalt-rich permanent-magnet materials is of paramount importance in materials science and technology since high-performance materials based on $Nd_2Fe_{14}B$ or FePt are extremely expensive or subject to limited rare-earth supplies.[1–4] Aside from phase-diagram considerations, this requires alloys with high magnetocrystalline anisotropy K_1 and Curie temperature T_c. However, the range of alternative compounds with appreciable K_1 and high T_c is limited, and the situation is often aggravated by their metastable nature and by the requirement of high-formation temperatures.[5–12] For example, two suitable candidates are Zr_2Co_{11} and $HfCo_7$, both crystallizing in noncubic structures, as necessary for high K_1. However, the poor control over phase purity in traditionally prepared bulk alloys has an adverse effect on permanent magnetic properties.[7,8,11,12] The future development requires high-performance magnetic materials for applications ranging from home appliances to sophisticated microelectronics and environment-friendly technologies, such as hybrid vehicles and wind turbines.[1–4]

Synthesis of magnetic materials in the form of nanoparticles smaller than 10 nm has emerged as an alternative method to stabilize traditional or new crystal structures.[13–17]

Small nanoparticles having high anisotropies also are essential as building blocks for high-energy nanocomposite magnets to ensure effective exchange coupling.[17–21] Wet-chemical and conventional physical vapor-deposition methods often require annealing at high temperatures to obtain the desired high-anisotropy crystal structures. In fact, this annealing step has been an important issue in controlling the size-distribution, self-assembly, easy-axis alignment, and nanostructure, not only in permanent magnetism but also in magnetic recording and other areas.[17–19,21–25] Easy-axis alignment of nanoparticles is particularly important to obtain high-energy products in permanent magnets because the energy product is quadratic in the magnetization. The annealing process and the associated sintering can be avoided by fabricating directly ordered nanoparticles using nonequilibrium cluster deposition, and this method can also be used to align the easy axes prior to deposition.[14–16] Here we show the fabrication of novel Zr_2Co_{11} permanent-magnet nanostructures in a single-step process using cluster-deposition method. Our structures are free of rare-earths and expensive Pt and exhibit record energy products for this class of materials.

A Zr-Co composite target of the required stoichiometry is sputtered using a direct-current magnetron discharge into a water-cooled gas-aggregation chamber.[15,16,26] The sputtered atoms gain sufficient energy via collisions with ions to form nanoparticles with high-anisotropy structures in the gas-aggregation chamber before deposition on substrates kept at room temperature in the deposition chamber. The Zr_2Co_{11} nanoparticles are monodisperse with an average particle size d = 8.7 nm and an rms standard deviation of σ/d = 0.18, as shown in the transmission electron microscopy (TEM) image (fig. 1a) and in the corresponding particle-size histogram of Zr_2Co_{11} nanoparticles (fig. 1b).

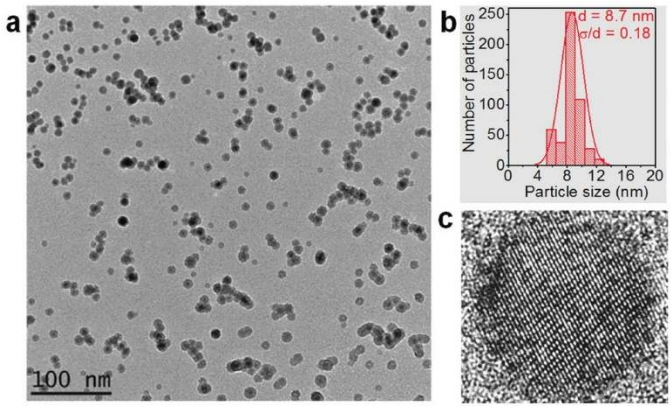

Figure 1. TEM analysis of Zr_2Co_{11} nanoparticles. (a) TEM image. (b) The particle-size histogram revealing a narrow size-distribution, where σ and d are the standard deviation and average particle size, respectively. (c) HRTEM image of a single nanoparticle showing a high degree of crystalline ordering.

High-resolution TEM (HRTEM) of a single Zr_2Co_{11} nanoparticle reveals a high degree of atomic ordering by showing lattice fringes (fig. 1c). Note that the nanoparticles were deposited with low coverage densities on carbon-coated copper grids only for TEM meas-

urements. For X-ray diffraction (XRD) and magnetic characterizations, thin-film assemblies of densely packed nanoparticles deposited onto a single-crystalline Si (001) substrate were used. The thickness of the films was varied from several nm to 1.4 μm by varying the deposition time (Supporting Information, Figure S1).

The red curve in figure 2a is the XRD pattern of a dense-packed Zr_2Co_{11} nanoparticle film deposited using the cluster deposition method. Bulk Zr_2Co_{11} alloys crystallize in rhombohedral or orthorhombic structures,[7,8] but the XRD pattern of Zr_2Co_{11} nanoparticles (red curve) is in good agreement with that of the rhombohedral bulk structure (blue curve) as shown in figure 2a.

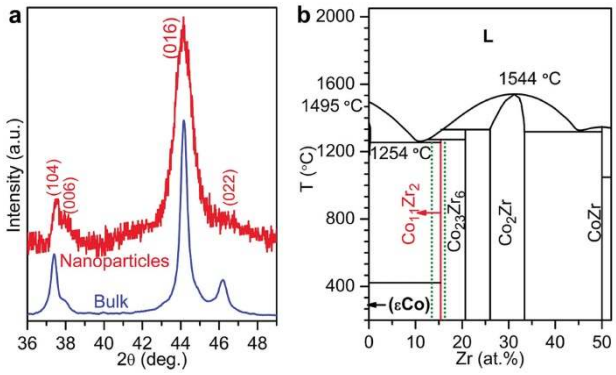

Figure 2. Phase formation of Zr-Co alloys. (a) The XRD pattern of Zr_2Co_{11} nanoparticle film deposited on a single crystalline Si (001) substrate is compared with that of rhombohedral bulk Zr_2Co_{11}. (b) Phase diagram.[5] The solid red vertical line represents the ideal composition and temperatures for the formation of Zr_2Co_{11} phase. The dotted green vertical lines show the composition region where the phase observed in nanoparticles is predominantly Zr_2Co_{11}.

Note that the Co-Zr bulk phase diagram, shown in figure 2b, indicates the formation of Zr_2Co_{11} equilibrium phase only at a single composition (solid red vertical line). However, in practice it is found that standard processing methods lead to the formation of secondary phases such as Co and Zr_6Co_{23} having low magnetocrystalline anisotropies during the cooling process.[7–9,11,12] The cluster-deposited Zr_xCo_{100-x} nanoparticles not only form in the high-anisotropy rhombohedral Zr_2Co_{11} structure for $x \approx 15.4$ without high-temperature annealing, but they also exhibit a predominant Zr_2Co_{11} phase for a rather broad composition region ($13.5 \leq \times \leq 16.3$), as indicated by green dotted vertical lines in figure 2b. This phase structure is also supported by magnetic measurements.

The direct crystalline ordering of Zr_2Co_{11} nanoparticles achieved during the gas-aggregation process in the present study is essential to align the easy axes of the nanoparticles in a magnetic field. Figure 3a shows the effect of a magnetic field ($H_{al} \approx 5$ kOe) applied before deposition on the Si substrate. The field H_{al} is applied along the x-direction, which is parallel to the substrate. The x-axis is therefore expected to be the easy magnetization direction, whereas both the y- and z-directions are hard directions.

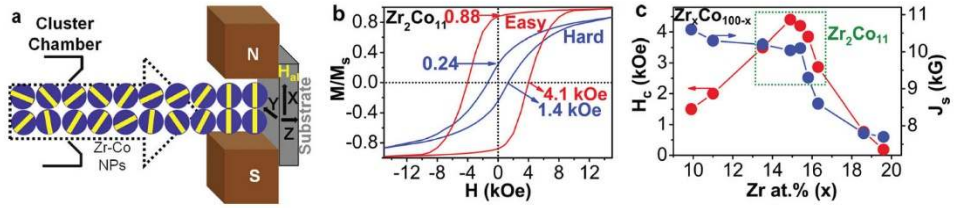

Figure 3. Magnetic properties of thin film assemblies of dense-packed nanoparticles. (a) Schematic of easy-axis alignment by applying a magnetic field (H_{al} ≈ 5 kOe) along the x-axis using a pair of permanent magnets (N-S). (b) Hysteresis loops for Zr_2Co_{11} measured at 300 K along the easy (x) and hard (y) axes. (c) Coercivity H_c and saturation polarization J_s measured along the easy axis at 300 K for Zr_xCo_{100-x}. The green-dotted rectangle shows the composition range where the phase is predominantly Zr_2Co_{11}.

Figure 3b shows the room-temperature magnetization M as a function of applied field H for aligned Zr_xCo_{100-x} nanoparticle film assemblies. The Zr_2Co_{11} films exhibit a high remanence ratio M_r/M_s and a high coercivity H_c along the easy axis, as compared with those along the hard axes. M_r and M_s are the remanent and saturation magnetizations, respectively. Figure 3c shows H_c and the saturation magnetic polarization ($J_s = 4\pi M_s$) of Zr_xCo_{100-x} nanoparticles as a function of Zr concentration x, measured along the easy axis. The figure yields H_c = 2.9–4.5 kOe and J_s = 8.6–10.2 kG for nanoparticle films that are predominantly Zr_2Co_{11}. These values are comparable to those of $SmCo_5$ and $L1_0$-ordered FePt and CoPt nanoparticles smaller than 10 nm.[13–17,24,25,27,28] Although nanoparticles are densely packed and stick to each other in the film, as shown in figure S1 in the Supporting Information, they nevertheless exhibit an appreciable room-temperature coercivity of about 4.5 kOe. This indicates that interparticle interactions and even physical contact do not destroy the coercivity.

Figure 4 shows the geometry and result of the alignment, which yields a high remanence ratio M_r/M_s = 0.88 along the easy axis, as compared to M_r/M_s ≈ 0.5 typically observed for randomly oriented nanoparticles.[29] For a noninteracting ensemble of uniaxial nanoparticles, the normalized average remanence can be written as:[29–34]

$$m_n = \frac{M_r}{M_s} = \frac{\int m(\theta)\, p(\theta) \sin\theta \, d\theta}{\int p(\theta) \sin\theta \, d\theta} \quad (1)$$

where θ is the angle between the easy-axis and x-direction, and m is the normalized magnetic moment of the individual nanoparticles in the field (or x-axis) direction. The easy-axis distribution or texture function $P(\theta)$ can be approximated by[30,34]

$$P(\theta) = P(0) \exp\left(\frac{\cos\theta}{\delta}\right) \quad (2)$$

In this equation, δ parameterizes the width of the easy-axis distribution ($\delta \ll 1$ for well-aligned particle ensembles).[30,31] Combination of Equation (1) and (2) yields M_r/M_s, which depends on δ. The remanence ratio of our Zr_2Co_{11} nanoparticles, M_r/M_s = 0.88, corresponds to a δ value of about 0.11 and to the narrow normalized distribution ($p(\theta) = P(\theta)/P(0)$), as

shown in figure 4b. Numerical evaluation of equation (1) shows that the percentage of nanoparticles with alignment angles smaller than 30° is about 73%.

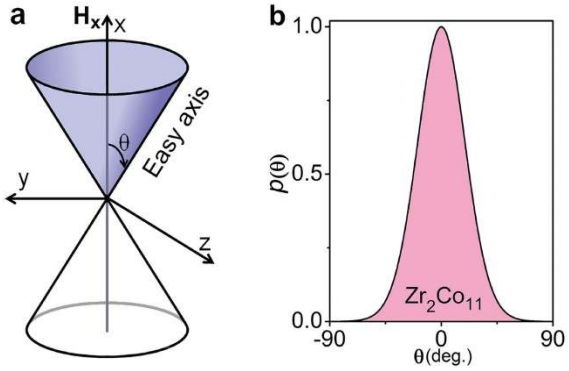

Figure 4. The normalized easy-axis probability distribution or texture function $p(\theta)$. (a) Geometric configuration, where H_x is the magnetic field applied along the x direction (direction of H_{al}) and θ is the angle between the easy axis and H_x. (b) $p(\theta)$ for aligned Zr_2Co_{11} nanoparticle assembly.

The energy product is a key figure of merit for a permanent-magnet material and is defined as the product of B and H_i in the second quadrant of the BH_i curve, where $B = H_i + 4\pi M$ and $H_i = H - NM_s$ are the magnetic field induction or flux density and the internal magnetic field, respectively. N is the demagnetization factor and estimated to be 0.26 for Zr_2Co_{11} nanoparticle films by comparing the slopes (micromagnetic susceptibilities) of in-plane and perpendicular $M(H)$ curves of isotropic samples (Supporting Information, Figure S2). Figure 5a shows the room-temperature B and energy-product (BH_i) curves for Zr_2Co_{11} nanoparticle films and yields a nominal energy product of about 16.6 MGOe. The packing fraction of nanoparticles in films is generally below full compaction, and thus, the energy products are normally evaluated using the mass of the magnetic materials and by assuming ideal density.[18] However, the volume fraction of the magnetic materials in these films can be improved via forming exchange-coupled nanocomposite by dispersing the nanoparticles in a magnetically soft matrix such as Fe-Co (Supporting Information S3). This nanostructure also improves the magnetic properties via exchange-coupling between hard and soft phases.[35,36] Note that the alignment of the hard phase is not affected by adding the soft phase and a remanence ratio of about 0.90 was obtained in the case of Zr_2Co_{11}:Fe-Co nanocomposites. In addition to the densification, Zr_2Co_{11}:Fe-Co nanocomposite film having 15 vol% soft Fe-Co phase, as shown in figure 5b, reveals an improvement in the energy product to 19.5 MGOe due to an increase of magnetization. Figure 5c illustrates the remarkable energy products of nanostructured Zr_2Co_{11} and Zr_2Co_{11}:Fe-Co (light colored bar) and shows that they are higher than those of the best alnico magnet and of the best low-cost rare-earth-free bulk materials (dark colored bars).[1,2,7,8,37–40]

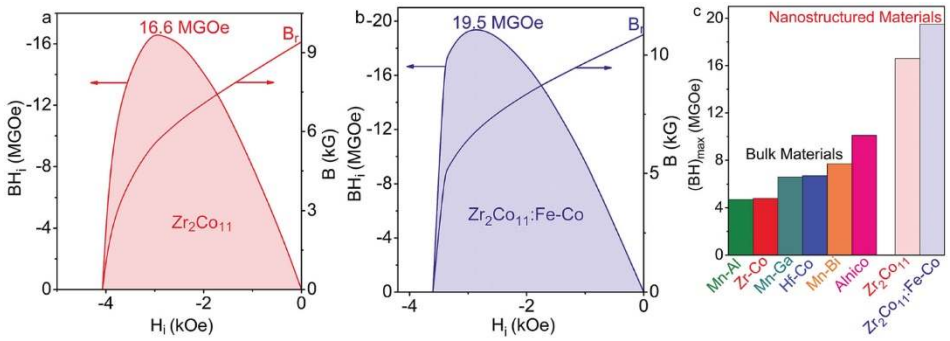

Figure 5. Energy products. *B* and BH_i curves for thin film assemblies: (a) Zr_2Co_{11} nanoparticles and (b) Zr_2Co_{11}:Fe-Co nanocomposites. (c) The energy products of nanostructured materials are given as light colored bars. For comparison, the energy products of alnico magnet and other rare-earth-free bulk materials reported in literature are plotted as dark colored bars. Data taken from refs.[1,2,7,8,37–40]

In conclusion, we have demonstrated the synthesis of new rare-earth-free Zr_2Co_{11} nanoparticles having high coercivity and magnetic moment using cluster-deposition, which are suitable as building blocks for rare-earth-free permanent-magnet materials. This method permits the direct ordering of high-anisotropy rhombohedral-structure nanoparticles without the requirement of a subsequent high-temperature annealing, alignment of the easy axes prior to deposition, and co-deposition of soft Fe-Co phase having high magnetization to fabricate exchange-coupled nanocomposites. The result is an assembly of a dense nanostructured rare-earth-free material in which a substantial magnetic remanence and coercivity are achieved, as well as the highest energy product for a non-rare-earth material. Nanostructured Zr_2Co_{11}-based materials, which remain to be fabricated in bulk forms, in due course, can be useful in applications, where magnets with energy products in the intermediate range between alnico and RE-containing magnets are required. Thus, the result reported in this study is an important step in mitigating the critical-materials aspects of rare-earth elements and satisfying the ever-increasing demand for permanent magnets.

Experimental Section

Zr_xCo_{100-x} ($10 \leq \times \leq 20$) nanoparticles were directly produced using the cluster-deposition method described elsewhere.[15,16] The experimental setup consisted of two chambers for cluster formation and deposition. The cluster-formation chamber had a direct current (DC) magnetron plasma-sputtering discharge with a water-cooled gas-aggregation tube, where Co and Zr atoms were sputtered from the Co-Zr target at a high dc magnetron sputtering power ($P_{dc} \approx 180$ W) using a mixture of argon (Ar) and helium (He) as sputtering gas to form Zr_xCo_{100-x} nanoparticles. The composition of the sputtering target was varied to tune the Zr concentration (x). The nanoparticles were extracted as a collimated beam moving toward the deposition chamber, and aligned by applying a magnetic field ($H_{al} \approx 5$ kOe) before deposition on substrates, which were kept at room temperature. The Zr_2Co_{11}:$Fe_{65}Co_{35}$ nanocomposite films were fabricated by co-depositing the easy-axis

aligned nanoparticles using the cluster source and a magnetically soft $Fe_{65}Co_{35}$ phase using another dc magnetron sputtering gun employed in the deposition chamber.

Nanoparticles were deposited on carbon-coated copper grids with low coverage densities to measure the average particle size and size distribution using an FEI Tecnai Osiris (scanning) transmission electron microscope. For the superconducting quantum interference device (SQUID) magnetometer, X-ray diffraction (XRD) (Rigaku D/Max-B diffractometer, where a Cu K wavelength of about 1.54 Å is used), and field-emission scanning electron microscopy (Hitachi S4700 FE-SEM and FEI Nova NanoSEM450) measurements, thin-film assemblies of densely packed nanoparticles were fabricated on single-crystalline Si (001) substrates. The mass (or nominal thickness) of the Zr_2Co_{11} nanoparticles films was measured using a quartz crystal thickness monitor. The thickness of the films was varied from several nm to 1.4 μm by varying the deposition time (Supporting Information, Figure S1). The nanoparticle samples were capped with a thin SiO_2 cap layer immediately after deposition, by using a radio-frequency magnetron sputtering gun employed in the deposition chamber.

Acknowledgments – This work was supported by Advanced Research Projects Agency-Energy (Grant No. DE-AR 0000046, B.B., D.J.S.), US Department of Energy (Grant No. DE-FG02–04ER46152, D.J.S., R.S., W.Z., B.D.), NSF (NSF-DMR-0960110, D.J.S.), and Nebraska Center for Materials and Nanoscience (Central Facilities). Thanks are due to Pinaki Mukherjee, V. R. Shah, X. Z. Li, Damien LeRoy, and Z. Sun for helpful discussions.

References

[1] N. Jones, *Nature* 2011, *472*, 22.

[2] J. M. D. Coey, *Scr. Mater.* 2012, *67*, 524.

[3] M. Jacoby, *Chem. Eng. News* 2013, *91*, 23.

[4] M. J. Kramer, R. W. McCallum, I. A. Anderson, S. Constantinides, *JOM* 2012, *64*, 752.

[5] H. Okamoto, *Phase Diagram of Binary Alloys*, ASM, Materials Park, OH 44073, USA, 2000, p. 263.

[6] H. Okamoto, *Phase Diagram of Binary Alloys*, ASM, Materials Park, OH 44073, USA, 2000, p. 248.

[7] G. V. Ivanova, N. N. Shchegoleva, A. M. Gabay, *J. Alloys Compd.* 2007, *432*, 135.

[8] W. Y. Zhang, X. Z. Li, S. Valloppilly, R. Skomski, J. E. Shield, D. J. Sellmyer, *J. Phys. D: Appl. Phys.* 2013, *46*, 135004.

[9] B. G. Demczyk, S. F. Cheng, *J. Appl. Cryst.* 1991, *24*, 1023.

[10] K. H. J. Buschow, *J. Appl. Phys.* 1982, *53*, 7713.

[11] T. Saito, *Appl. Phys. Lett.* 2003, *82*, 2305.

[12] Z. Hou, W. Wang, S. Xu, J. Zhang, C. Wu, F. Su, *Phys. B.* 2012, *407*, 1047.

[13] S. Stappert, B. Rellinghaus, M. Acet, E. F. Wassermann, *J. Cryst. Growth.* 2003, *252*, 440.

[14] J. M. Qiu, J. P. Wang, *Appl. Phys. Lett.* 2006, *89*, 222506.

[15] B. Balasubramanian, R. Skomski, X. Z. Li, S. R. Valloppilly, J. E. Shield, G. C. Hadjipanayis, D. J. Sellmyer, *Nano. Lett.* 2011, *11*, 1747.

[16] B. Balamurugan, B. Das, V. R. Shah, R. Skomski, D. J. Sellmyer, *Appl. Phys. Lett.* 2012, *101*, 122407.

[17] B. Balamurugan, D. J. Sellmyer, G. C. Hadjipanayis, R. Skomski, *Scr. Mater.* 2012, *67*, 542.

[18] H. Zeng, J. Li, J. P. Liu, Z. L. Wang, S. Sun, *Nature* 2002, *420*, 395.

[19] D. J. Sellmyer, *Nature* 2002, *420*, 374.

[20] X. Liu, S. He, J. M. Qiu, J. P. Wang, *Appl. Phys. Lett.* 2011, *98*, 222507.

[21] N. Poudyal, J. P. Liu, *J. Phys. D: Appl. Phys.* 2013, *46*, 043001.

[22] S. Sun, C. B. Murray, D. Weller, L. Folks, A. Moser, *Science* 2002, *287*, 1989.

[23] D. Alloyeau, C. Ricolleau, C. Mottet, T. Oikawa, C. Langlois, Y. LeBouar, N. Braidy, A. Loiseau, *Nat. Mater.* 2009, *8*, 940.

[24] S. Kang, Z. Jia, S. Shi, D. E. Nikles, J. W. Harrell, *Appl. Phys. Lett.* 2005, *86*, 062503.

[25] S. Kang, S. Shi, Z. Jia, G. B. Thompson, D. E. Nikles, J. W. Harrell, D. Li, N. Poudyal, V. Nandwana, J. P. Liu, *J. Appl. Phys.* 2007, *101*, 09J113.

[26] H. Haberland, M. Moseler, Y. Qiang, O. Rattunde, Th. Reiners, Y. Thurner, *Surf. Rev. Lett.* 1996, *3*, 887.

[27] T. Matsushita, T. Iwamoto, M. Inokuchi, N. Toshima, *Nanotechnology* 2010, *21*, 095603.

[28] C. H. Chen, S. J. Knutson, Y. Shen, R. A. Wheeler, J. C. Horwath, P. N. Barnes, *Appl. Phys. Lett.* 2011, *99*, 012504.

[29] (a) E. P. Wohlfarth, *J. Appl. Phys.* 1958, *29*, 595; (b) C. Tannous, J. Gieraltowski, *Eur. J. Appl. Phys.* 2008, *29*, 475.

[30] D. LeRoy, R. Morel, A. Brenac, L. Notin, *J. Mag. Mag. Mat.* 2011, *323*, 127.

[31] L. Néel, R. Pauthenet, G. Rimet, V. S. Giron, *J. Appl. Phys.* 1960, *31*, 27S.

[32] H. Rubio, S. Suárez, *J. Appl. Phys.* 2000, *87*, 7415.

[33] K. H. Müller, D. Eckert, P. A. P. Wendhausen, A. Handstein, S. Wirth, M. Wolf, *IEEE Trans. Magn.* 1993, *30*, 586.

[34] D. Givord, A. Lignard, R. Perrier de la Bathie, P. Tenaud, T. Viadieu, *J. Phys. Colloques* 1985, *C6*, 313.

[35] E. F. Kneller, R. Hawig. *IEEE Trans. Magn.* 1991, *27*, 3588.

[36] R. Skomski, J. M. D. Coey, *Phys. Rev. B.* 1993, *48*, 15812.

[37] J. H. Park, Y. K. Hong, S. Bae, J. J. Lee, J. Jalli, G. S. Abo, N. Neveu, S. G. Kim, C. J. Choi, J. G. Lee, *J. Appl. Phys.* 2010, *107*, 09A731.

[38] B. Balke, G. H. Fecher, J. Winterlik, C. Felser, *Appl. Phys. Lett.* 2007, *90*, 152504.

[39] M. A. McGuire, O. Rios, N. J. Ghimire, M. Koehler, *Appl. Phys. Lett.* 2012, *101*, 202401.

[40] J. B. Yang, K. Kamaraju, W. B. Yelon, W. J. James, Q. Cai, A. Bollero, *Appl. Phys. Lett.* 2001, *79*, 1846.

Supporting Information

Supporting Information S1

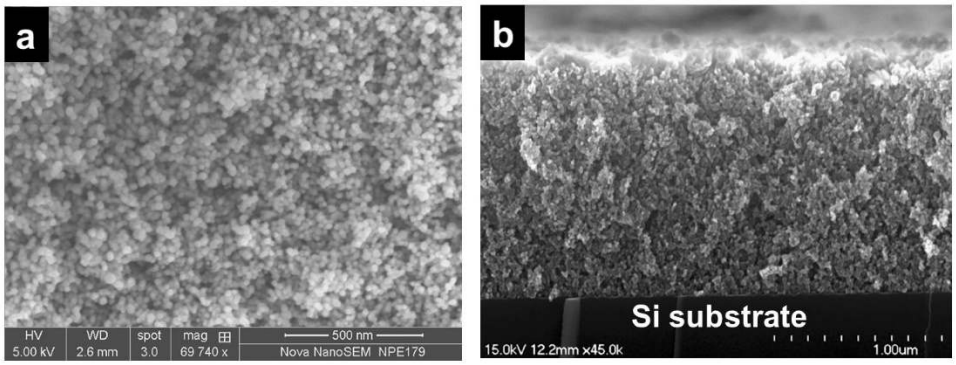

Figure S1. FESEM images of Zr_2Co_{11} nanoparticle films deposited on Si (001). (a) Top view. (b) Cross-sectional view, showing that the film has a thickness of about 1.4 μm. For the cross-sectional imaging, the sample was prepared by cutting the Si substrate after deposition.

The secondary-electron (FESEM) images of figure S1 shows that our films are fairly dense; that is, they do not consist of loosely packed spheres. The volume fraction is difficult to determine from the cross-sectional view due to roughness or pores generated during the cleaving process and are generally between 50 and 80% for different cluster-deposited nanoparticle samples. In particular, smaller nanoparticles fill interstitial holes between bigger nanoparticles. However, the density of the Zr_2Co_{11} nanoparticle films estimated from the thickness and mass of the samples is about 70%.

Supporting Information S2

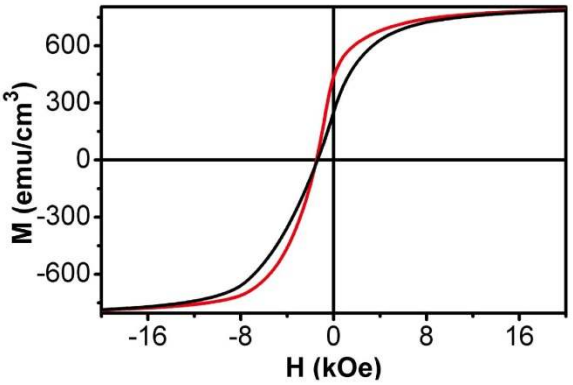

Figure S2. Room-temperature hysteresis loops for an isotropic ensemble of Zr_2Co_{11} nanoparticles measured along the in-plane or *x* (red) and out-of-plane or *z* (black) directions.

The demagnetization factor N_x has been estimated from figure S2, using $Nx + Ny + Nz = 1$ and $Nx = Ny$ for the two in-plane directions, $2Nx + Nz = 1$.[1,2] The individual magnetization factors N_i (i = x, y, z) are related to the external magnetic susceptibilities χ_i by $1/\chi_i = 1/\chi_o + N_i$, where χ_o is independent of sample shape.[3] Extracting the two susceptibilities (loop slopes) χ_x and χ_z from figure S2, we obtain $N_x \approx 0.26$. Similar analysis yields a comparatively low $Nx \approx 0.15$ for nanocomposite films.

References

[1] G. Zheng, M. Pardavi-Horvath, X. Huang, B. Keszei, J. Vandlik, *J. Appl. Phys.* 1996, *79*, 5742.

[2] R. Skomski, *Simple Models of Magnetism*, Oxford University Press, 2008.

[3] J. M. D. Coey, *Magnetism and Magnetic Materials*, Cambridge University Press, 2009.

Supporting Information S3

Figure S3 shows that cluster deposition can be used to realize high packing fractions approaching f ≈ 1 in magnetic nanoparticle systems. We have fabricated the Zr_2Co_{11}:Fe-Co nanocomposite films by co-depositing Zr_2Co_{11} nanoparticles using the cluster source and $Fe_{65}Co_{35}$ phase using another dc magnetron sputtering gun employed in the deposition chamber. The image shows that Zr_2Co_{11} nanoparticles are coated and surrounded by $Fe_{65}Co_{35}$ to form a dense-packed magnetic material.

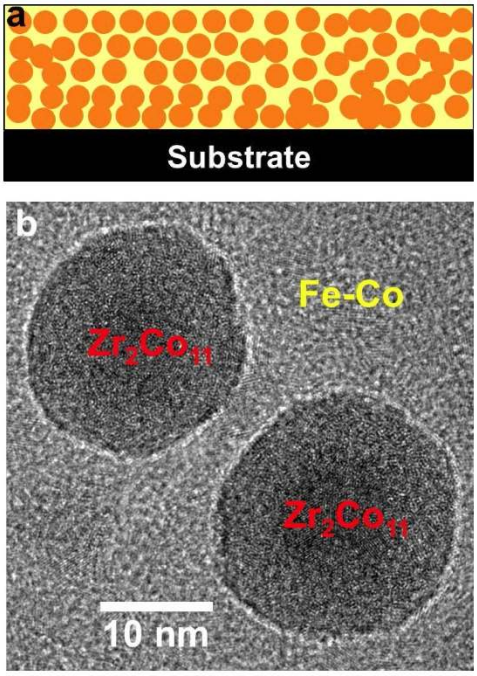

Figure S3. Nanocomposite films: (a) A schematic of nanoparticles (red) dispersion in a magnetically soft (yellow) matrix. (b) HRTEM image Zr_2Co_{11}:Fe-Co showing nanoparticles coated and surrounded by Fe-Co phase. The nanoparticles were deposited with low coverage densities in order to show clearly the coating of Fe-Co.